



Basin stability for updating system uncertainties

Dawid Dudkowski  and Tomasz Kapitaniak 

Division of Dynamics, Lodz University of Technology, Stefanowskiego 1/15, 90–537 Lodz, Poland



(Received 24 October 2023; accepted 28 June 2024; published 17 July 2024)

In this paper, we propose an application of the basin stability tool which allows us to update the information on the system properties under parameter uncertainties. The concept is presented using a classical mechanical setup of coupled pendula, exchanging the energy via the supporting structure. Depending on the support parameters, the model can exhibit different types of coexisting synchronous patterns as well as remaining desynchronized. We calculate basin stability maps of particular behaviors and combine them with prior parameter distributions using Bayesian inference. The obtained posterior distributions, based on the attractor occurrence, update our knowledge on the system properties in the terms of probabilities. We also underline the problem of evaluating basin stability close to the existence borders, comparing the classical approach of fixed parameters with the one involving variations. The differences between the estimation methods can have a crucial meaning for the discussed application and should be considered carefully. The results presented in this paper uncover ways of applying the basin stability concept, which can be used to study the properties of complex dynamical systems from a probability perspective.

DOI: [10.1103/PhysRevE.110.014205](https://doi.org/10.1103/PhysRevE.110.014205)

I. INTRODUCTION

The concept of *basin stability* introduced by Menck *et al.* [1] contributes to modern ways of investigating complex dynamical systems. In its various applications, the tool allows us to compare the probabilities of the occurrence between different attractors of multistable models, predict (and possibly limit) rare solutions, or evaluate states robustness to perturbations.

Among the variety of systems where basin stability has been studied, one can indicate climate [2] and epidemic [3] models, food chains [4], coupled oscillators [5–7], or delayed dynamics [8], just to mention a few.

In Ref. [9], the authors discussed the concept from a stochastic perspective, focusing on the vegetation-water system subjected to Gaussian noise. The application of the basin stability for studying transient phenomena can be found in Ref. [10], where van Kan *et al.* applied it in the paradigmatic Lorenz system to investigate the boundary crisis bifurcation. The tool allows us to identify and quantify chimera states [11], making it a good precursor for studying complex behaviours in nonlinear systems.

A large portion of research in this topic refers to power grids [12], where the stability of generator-consumer relation is crucial for the network to work properly (see, e.g., Ref. [13]). The results published so far include transient problems [14,15], where the authors estimated the regions of attraction through time-domain simulations. The phenomenon of tripping time effects in heterogeneous networks has been discussed in Ref. [16], while in Refs. [17,18] the research is focused on limited-size models. The analysis of correlations between basin stability and other grid measurable quantities can be found in Ref. [19], where Feld and Hartmann exhibited that the tool can be effectively used to analyze perturbations occurring within the system. The basin

stability concept evolved in time and allowed introducing various related derivatives, e.g., finite-time [20] or multiple-node [21] basin stabilities. In Ref. [22], Ji *et al.* investigated the stochastic variation, applying it to study the dynamics under the influence of random noise. The evolution of the tool underlines that the measures based on the original basin stability idea can be adopted to study the behaviors of complex systems from a probability perspective.

The experimental confirmation of the concept has been presented in Refs. [23,24], involving classical mechanical rigs of coupled oscillators. The results show that the probability approach can become a potential alternative to the bifurcation analysis, leading to similar results. Also, the growing development of machine-learning methods contributes to the field, leading to faster and more efficient estimations using vector machines [25,26] or neural networks [27]. The application of modern classification methods can drastically reduce the time required for the basin stability estimation, which can become crucial for high-dimensional models with many coexisting attractors where the computational cost of classical sampling is significant. The application of the concept also has other limits and constraints, e.g., when the geometry of the basins become fractal or riddled; see Ref. [28] by Schultz *et al.* for details.

As described above, the basin stability concept has been applied and developed in various types of nonlinear problems, showing that the occurrence of the attractors within a given system can be discussed from a probability perspective. By applying the tool in complex models, we can estimate random appearances of crucial solutions and possibly control (or induce) them. The problem is closely related to the parameters of the considered system, since the coefficients determine the regions where the attractors reside. However, the knowledge on the parameters is not always fully known (especially in real-life complex systems) and some prior assumptions on

their distribution have to be stated. In such a scenario, we can utilize the basin stability maps for updating our assumptions, obtaining the posterior parameter distribution which involves the probabilistic measures of possible solutions. Such an update can be further used to determine the conditions that have led to the occurrence of particular behaviors and predict it in the future with higher accuracy. In this manner, the procedure discussed in this paper uncovers another application of the basin stability tool, exhibiting that it can be used to update the information on system parameters and consequently decrease the uncertainty level of the considered model.

II. THE PROCEDURE AND THE RESULTS

Let us consider a general system of ordinary differential equations (ODEs) determined by vector field f ,

$$\dot{y} = f(y, \gamma^*, t), \quad (1)$$

where $y \in Y$ and $\gamma^* \in \Gamma$. Sets Y and Γ correspond to the phase space and the parameters space, respectively, while $t \geq 0$ denotes the dynamical time (the y variable evolves in time, while the parameters vector γ^* is fixed). For clarity, in this paper we focus on simple ordinary differential equations models for which the original basin stability tool has been introduced [1]. However, since basin stability methods and concepts have been successively developed in various types of dynamical problems of different structures (e.g., the ones including delays [8] or random noise [22]), the procedure proposed in this paper could be translated into other models governed by more complex equations.

The implementation of Eq. (1) can be realized in various ways, depending on the nature of the considered dynamical problem. In this paper, we study the example of classical mechanical setup which is shown in the upper part of Fig. 1. The system is focused on pendula elements and, as we have shown in previous works (see, e.g., Refs. [29,30]), it realizes typical states found for coupled oscillators, including synchronization patterns or chaotic motion. The pendula and their behaviors are fundamental for the dynamics of various mechanisms and machines, and their proper understanding contributes to modern mechanical engineering research. As we discuss in this paper, the procedure of determining posterior parameter distribution based on the basin stability concept can be effectively applied for classical pendula schemes, leading to additional ways of investigating more complex mechanical setups.

The system of three degrees of freedom shown in Fig. 1 includes the movable beam of mass $M_x = 6.0$ (kg) (dynamical variable $x \in \mathbb{R}$) which holds two identical pendula clocks of masses $m = 1.0$ (kg) and lengths $l = 0.24849$ (m) (variables $\varphi_1, \varphi_2 \in (-\pi, \pi]$). The beam is connected with the unmovable support using the spring of stiffness k_x and the damper characterized by coefficient c_x .

The dimensionless equations of motion of the discussed model are given as follows:

$$\begin{aligned} \ddot{x} + \alpha_x^2 x + 2h_x \dot{x} + \mu \sum_{i=1}^2 (\ddot{\varphi}_i \cos \varphi_i - \dot{\varphi}_i^2 \sin \varphi_i) &= 0 \\ \ddot{\varphi}_i + \alpha_\varphi^2 \sin \varphi_i + 2h_\varphi \dot{\varphi}_i + \lambda \dot{x} \cos \varphi_i &= \hat{M}_i. \end{aligned} \quad (2)$$

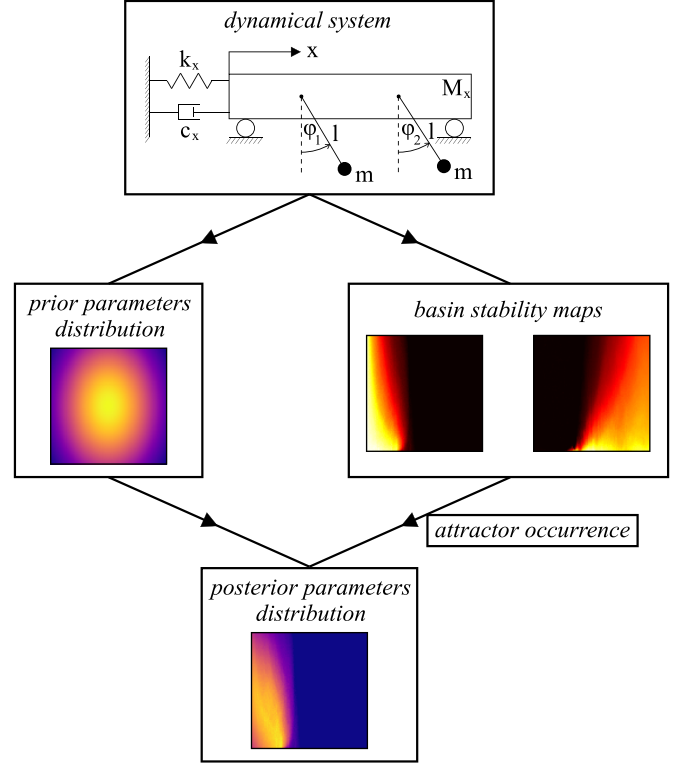


FIG. 1. The scheme of the discussed concept. The procedure begins with the determination of the model of interest (see the upper part of the figure; in this paper, we focus on the mechanical setup of three degrees of freedom). Given the system, we can assume the prior distribution of its parameters and calculate the basin stability maps of possible attractors; see the middle part of the figure where the results are presented for two-dimensional parameter vectors. Combining prior PDF and basin stability in the presence of particular attractor, we can finally calculate the posterior parameters distribution (as shown in the lower part of the figure). The arrows indicate the route within which the information on the system parameters is being updated.

The equations given in (2) originate from the Lagrange methodology and involve second-order ordinary differential equations. By splitting the original variables x and φ_i into the displacement ($x_1 = x$, $\varphi_{i,1} = \varphi_i$) and the velocity ($x_2 = \dot{x}$, $\varphi_{i,2} = \dot{\varphi}_i$) components, we can easily transform model (2) into the system of first-order ODEs:

$$\begin{aligned} \dot{x}_1 &= x_2 \\ \dot{x}_2 &= -\alpha_x^2 x_1 - 2h_x x_2 - \mu \sum_{i=1}^2 (\dot{\varphi}_{i,2} \cos \varphi_{i,1} - \varphi_{i,2}^2 \sin \varphi_{i,1}) \\ \dot{\varphi}_{i,1} &= \varphi_{i,2} \\ \dot{\varphi}_{i,2} &= -\alpha_\varphi^2 \sin \varphi_{i,1} - 2h_\varphi \varphi_{i,2} - \lambda \dot{x}_2 \cos \varphi_{i,1} + \hat{M}_i. \end{aligned} \quad (3)$$

In this case, the vector variable y in Eq. (1) equals $y = (x_1, x_2, \varphi_{1,1}, \varphi_{1,2}, \varphi_{2,1}, \varphi_{2,2})$.

For the purpose of the research, we have fixed the following parameters of system (2): $\mu = ml/(M_x + 2m) = 0.031061$, $\alpha_\varphi^2 = g/l = 39.47845$, $h_\varphi = c_\varphi/(2ml^2) = 0.080975$ (where $c_\varphi = 0.01$ [Nms] is the linear damping of the pendula), and $\lambda = 1/l = 4.02431$. The excitation of the system is induced

by function $\hat{M}_i = M_{\text{ext}}^i/(m l^2)$, where M_{ext}^i describes the external momentum driving the i th clock and is associated with the escapement mechanism coefficients $M_F = 0.075$ (nm) (the moment of force) and $\varepsilon = 5.0^\circ$ (the escapement deactivation threshold). The considered mechanism can be classically found in metronomes and clocks (see, e.g., Refs. [29,31] for details) and strictly depends on the pendula position φ_i : when the unit displacement exceeds the escapement deactivation threshold ε , the mechanism turns off and there is no excitation applied; otherwise, the unit is excited by constant moment of force M_F .

System (1) can possess various coexisting attractors (the multistability property) which can appear or disappear if the parameters are varied. From a technical point of view, the qualitative changes are more crucial than the quantitative ones, so in this paper we consider the family of solutions of a particular type as one representative state (e.g., the in-phase synchronization of the pendula, which remains stable for various parameters but involves different amplitudes).

Let A^* be the attractor of system (1) (for fixed γ^*). According to the original concept proposed in Ref. [28], the basin stability of A^* is defined as

$$\mathcal{S}_{B(A^*)} := \mu(\mathcal{B}(A^*)), \quad (4)$$

where μ is the measure encoding the frequency of system perturbations (the basin stability of an attractor is the probability measure of its basin of attraction). Since the attractor (its representative state) can exist for various values of parameters, a practical realization of the concept leads to *basin stability maps*, where we determine the stability of the basins within full Γ space.

To underline the variability of system parameters, we propose to express the basin stability in terms of conditional probability, namely, let A denote the random variable that determines the system attractor, while G is the random variable (vector) describing the system parameters (G takes values in Γ). We have

$$\mathcal{S}_{B(A^*)} = P_\mu(A = A^* | G = \gamma^*), \quad (5)$$

where the probability of observing attractor A^* is conditioned on parameters vector γ^* (we calculate the probability of the occurrence of A^* knowing that the parameters are fixed at γ^*). Variables A and G are naturally dependent, since the basin stability of any attractor highly depends on the parameter values. The μ measure in formula (5) is used to determine probabilities; in this paper we consider it as the uniform one for simplicity.

The distribution of G random variable depends on the type of dynamical system. If the parameters can be precisely determined, then G denotes a discrete, probability mass point function. However, in many practical scenarios the shape of G is not so explicit, e.g., due to limitations in measurements or the possibility of rare and extreme events [32]. In such cases, we can assume the prior parameters distribution of G (see the left middle part in Fig. 1), which is based on the properties of the considered model (the meaning of its parameters and their possible values). On the other hand, using the classical methods of basin stability estimation [1,28], we can also calculate the maps for possible system attractors, expressing

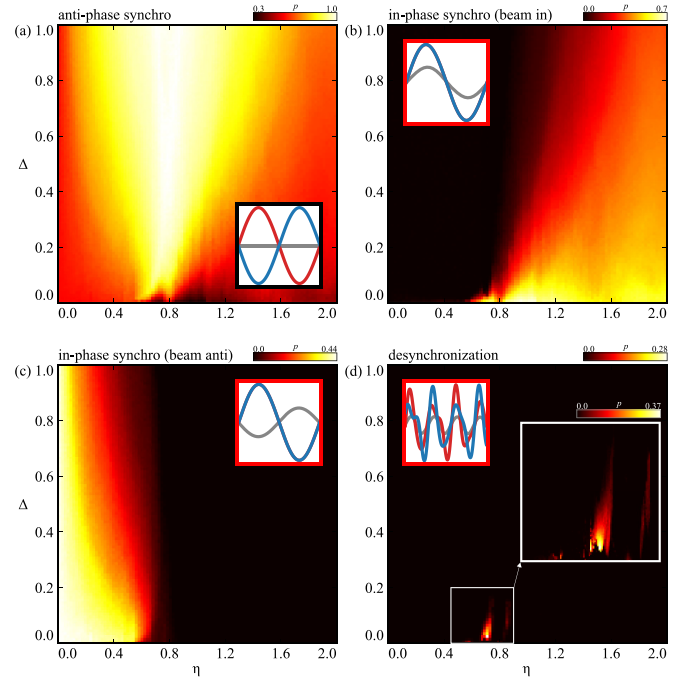


FIG. 2. The basin stability maps of system (2) in (η, Δ) parameter plane. Each subfigure corresponds to different oscillatory patterns, including three synchronization scenarios, (a)–(c), and the desynchronization case, (d), also enlarged for higher resolution. The schemes of motion within the states are shown in the white insets, where the pendula are marked in red and blue, while the beam is shown in grey. The brighter the color, the higher the basin stability of a particular state (the probability of the occurrence is denoted by parameter p in the color bars)

them in the same Γ parameter space (see the right middle part in Fig. 1). It should be noted that the results presented in the figure are schematic and aimed to introduce the general idea of the discussed procedure; the detailed example of application can be found in Figs. 2 and 3.

Both prior parameter distribution and basin stability maps depend on the type of the considered dynamical problem and can be derived from the model, which is marked by the upper arrows in Fig. 1. The scheme shown in the figure represents an exemplary case of two-dimensional Γ parameter space and the basin stability maps of two possible attractors. To distinguish between the results, we have used different color scales which indicate the density of distribution (the left middle panel) and the basin stability maps (the probabilities of solution occurrence; the right middle panel).

Combining the prior distribution of G and the maps within the formulation of basin stability (5), we can update the knowledge on system properties under uncertainties; namely, using Bayes' theorem and the law of total probability, we have

$$\begin{aligned} p_G(\gamma^* | A = A^*) &= \frac{P_\mu(A = A^* | G = \gamma^*) p_G(\gamma^*)}{P_\mu(A = A^*)} \\ &= \frac{\mathcal{S}_{B(A^*)} p_G(\gamma^*)}{\int_\Gamma P_\mu(A = A^* | G = \gamma) p_G(\gamma) d\gamma}, \quad (6) \end{aligned}$$

where $p_G(\gamma^* | A = A^*)$ is the posterior parameter distribution of G [in the form of probability density function (PDF)],

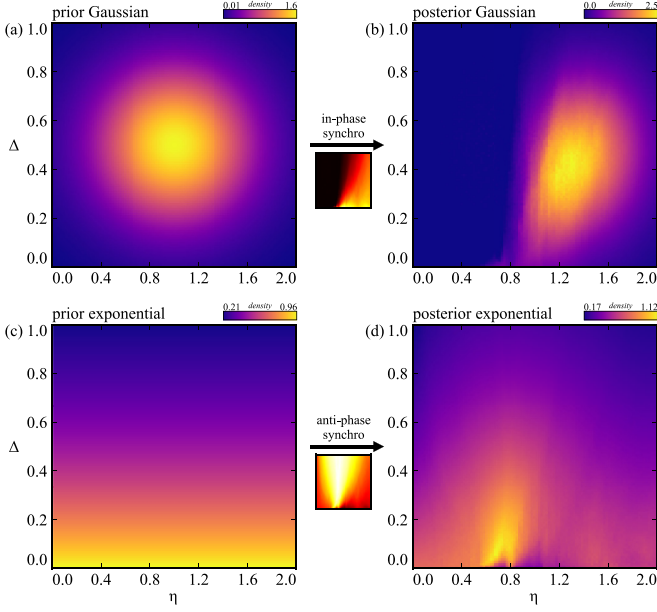


FIG. 3. The prior parameter distributions (left panel) and their posterior counterparts (right panel) after updating the basin stability maps of chosen attractors (the middle insets). In the upper row [(a), (b)], we present the transformation of the Gaussian distribution (parameters $\mu_\eta = 1.0$, $\sigma_\eta = 0.2$, $\mu_\Delta = 0.5$, $\sigma_\Delta = 0.05$, $\rho_{\eta\Delta} = 0$) in the case of the in-phase synchronization occurrence (with the beam in the in-phase to the pendula). The scenario of the exponential distribution (with parameter $\lambda = 1.5$) and the antiphase pattern is shown in the lower row [(c), (d)]. The brighter the color, the higher the values of the probability density functions.

conditioned on the observance of particular A^* attractor. The shape of the posterior $p_G(\gamma^*|A = A^*)$ is based on the form of the prior assumption $p_G(\gamma^*)$ and the basin stability map of the chosen state: $\mathcal{S}_{B(A^*)}$. This relation is shown in the lower part of Fig. 1, where the left arrow corresponds to the prior p_G assumption, while the right one corresponds to the basin stability map of the observed attractor (we can examine how the distribution updates in various scenarios of attractor occurrence). Combining both the prior probability distribution and basin stability map, we obtain the posterior distribution of the system parameters.

If the system is monostable within the Γ space, then $P_\mu(A = A^*|G = \gamma^*) = 1 = P_\mu(A = A^*)$ and $p_G(\gamma^*|A = A^*) = p_G(\gamma^*)$, i.e., we get no new information from probabilities. A similar case occurs when the model possesses various solutions (depending on the parameter values), but there is no coexistence between them; in such a scenario, the posterior distribution is reduced to the region of existence of the A^* state and scaled by the $P_\mu(A = A^*)$ probability. However, if the model exhibits at least bistability between the solutions, then formula (6) can be used to update system uncertainties. In the most trivial case, when the prior $p_G(\gamma^*) = \text{const}$ (the uniform scenario), we can use the basin stability map itself to collect the posterior distribution, since the presumed probability of the occurrence of every parameter is the same. When considering more complex prior scenarios, the basin stability map combines with the shape of $p_G(\gamma^*)$, allowing us to gather insights on the conditions leading to the state. In this sense, the

observance of the attractor updates the uncertainties related to the distribution of parameters.

The whole procedure shown in Fig. 1 can be traced using the arrows included. First, we determine the system of interest (the upper part). Then, based on the model, we can assume its prior parameter distribution (the left middle panel) and calculate the basin stability maps of its possible attractors (the right middle panel). Finally, relation (6) allows us to collect the updated posterior distribution of the parameters (the lower part), relaying the information from the prior parameter assumption which is conditioned on the occurrence of the particular attractor.

To study the tool for the model determined by Eq. (2), we focus on its suspension properties. The main part of the system—the beam with the hanged pendula—can be considered as a mechanical rig connected with the environment, i.e., there is some relation between the system and the external environment, which is expressed by the suspension parameters: the spring stiffness k_x and the damper coefficient c_x (see the scheme in the upper part in Fig. 1). The exact values of the parameters can be unknown but we may assume their prior distributions based on various conditions (e.g., the higher damping can be less probable than the lower one or the distributions can be unimodal).

Referring to Eq. (2), the dimensionless parameters correspond to the dimensional ones in the following way: $\alpha_x^2 = k_x/(M_x + 2m)$ and $h_x = c_x/2(M_x + 2m)$. From a practical point of view, we introduce two coefficients which qualitatively describe the vibrations conditions of the model. The η parameter will denote the ratio between the oscillations frequency of the beam with suspended pendula and the vibrations frequency of the pendula themselves, i.e., $\eta = \alpha_x/\alpha_\varphi$. When $\eta < 1.0$, the beam-spring setup is above the resonance; otherwise it is below. The second parameter, $\Delta = 2h_x\pi/\alpha_x$, describes the logarithmic decrement of the model. When $\Delta < 0.5$, the beam-spring system is weakly damped, otherwise the damping is strong. Both η and Δ coefficients will be varied and considered uncertainties in the system [$\gamma = (\eta, \Delta)$; see Eq. (1) for details]. The model shown in Fig. 1 can exhibit different types of synchronization between the pendula and the beam as well as remaining desynchronized. For each of the possible states, we have calculated the basin stability maps, which are presented in Fig. 2.

The construction of the maps is based on the discretization of the parameters space $\Gamma = \{(\eta, \Delta) : \eta \in [0.0, 2.0], \Delta \in [0.0, 1.0]\}$. The intervals for both coefficients have been partitioned into 100 subintervals of equal size, resulting in 100×100 mesh in total. For each cell of the mesh, we have performed a series of trials, varying uniformly both the initial conditions of the system and the values of the parameters within the cell (this approach differs from the classical one, when the parameters are fixed—usually considered the center point of the cell; see also the discussion in Figs. 4 and 5 for details). By determining the result of each trial (the attractor to which the system converged), we have estimated the stabilities of the states and distinguished the regions of their more and less probable occurrences. The results are based on 1000 trials for each cell, i.e., 10 000 000 trials in total.

In Fig. 2(a), one can see the basin stability map of the antiphase synchronization pattern which exists in the full

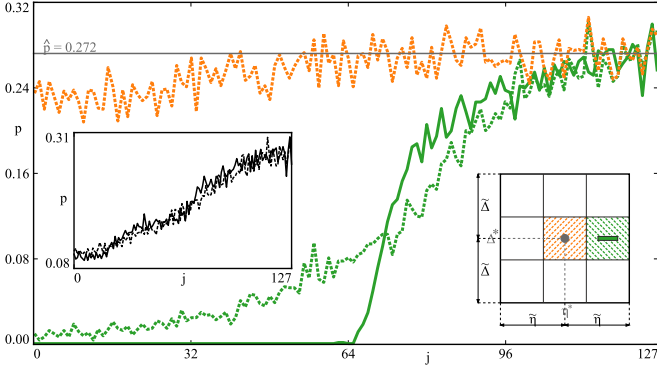


FIG. 4. The estimations of basin stability of the desynchronization solution using the classical approach of parameters fixed (the solid curves) and the method of parameters varied (the dashed curves). The orange and green patterns correspond to the parameters from the hatched cells included in the inset, while the black ones correspond to the full 3×3 matrix. Indicator j determines the size of the parameter matrix which is centered around the grey point $(\eta^*, \Delta^*) = (0.70875, 0.015)$, with lengths $\bar{\eta} = 0.008 - j \times 6.25 \times 10^{-5}$ and $\bar{\Delta} = 0.0032 - j \times 2.5 \times 10^{-5}$. The basin stability for the center has been estimated as $\hat{p} = 0.272$

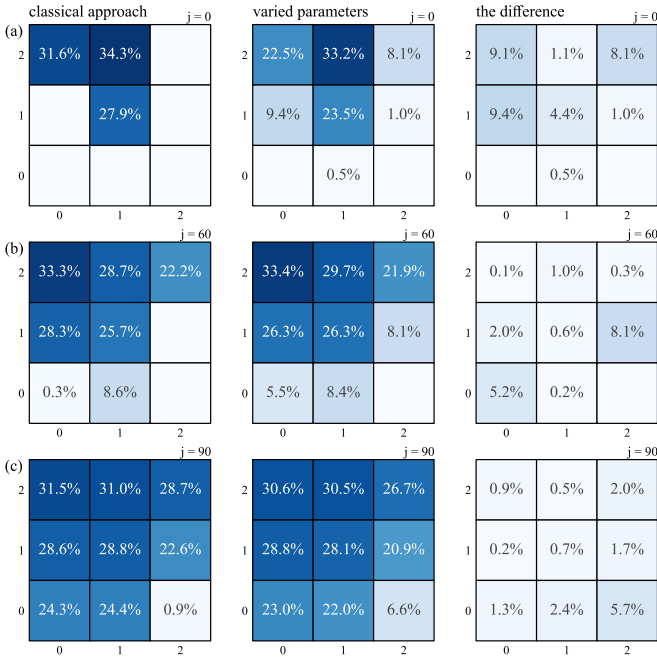


FIG. 5. The comparison of basin stability between the classical approach with parameters fixed (the left column) and the proposed one with parameters varied (the middle column). The results shown in the rows (a)–(c) correspond to different sizes of the parameters matrix included in the inset of Fig. 4: (a) $j = 0$, (b) $j = 60$, and (c) $j = 90$. Each of the matrices shown is centered around fixed $(\eta^*, \Delta^*) = (0.70875, 0.015)$ point and contains the estimations of the basin stability of the desynchronization solution within 3×3 regime mesh (the darker the color, the higher the probability; the domains of the absence of the state are left blank). For easier reference to the cells within particular matrix, the rows and columns are equipped with indices 0, 1, 2. The right column includes the absolute difference between the results obtained using both methods for comparison.

parameter range. The results included in the inset (see also the ones in the other panels of Fig. 2) schematically show the evolution of the pendula and the beam in time. The red and blue curves denote the time plots of the pendula, which in the considered case oscillate in the antiphase: $\varphi_1 = -\varphi_2$ (the inset includes one full cycle of motion). Due to the stable balance between the oscillators, the beam (shown in grey) does not move: $x = 0$.

The color scale used to illustrate basin stability (marked as parameter p) indicates the higher (lower) probabilities with the brighter (darker) color. In this scenario, one can observe the funnel centered around $\eta = 0.8$, where the antiphase pattern is the most probable one ($p \approx 1$). The lowest observed basin stability ($p \approx 0.3$) resides close to the resonance region: $\eta \approx 1.0$, when the damping is very small ($\Delta \approx 0$).

System (2) also possesses two in-phase synchronization solutions (when $\varphi_1 = \varphi_2$), which are discussed in Figs. 2(b) and 2(c). The states can be distinguished by the behavior of the beam in which oscillations have been magnified in the insets for better visualization. In the Fig. 2(b) case, the platform (grey) is oscillating in the in-phase to the synchronized pendula (see the blue curve overlapping the red one and the grey curve with the extremes on the same side as for the pendula: $\text{sign}(\varphi_i) = \text{sign}(x)$). In the Fig. 2(c) scenario, the motion of the platform is realized in the antiphase to the nodes—the extremes of the grey and the blue curves are on opposite sides: $\text{sign}(\varphi_i) = -\text{sign}(x)$. Both patterns can be also identified by their basin stability maps—the Fig. 2(b) state (with the beam in) resides mainly above $\eta > 0.8$ (with the highest probability $p \approx 0.7$ for smaller Δ damping), while the Fig. 2(c) state (with the beam anti) can be found below the $\eta < 0.8$ threshold.

Apart from synchronous motion, the considered system can also remain destabilized, which is possible within a very small domain of parameters in Fig. 2(d). In this case, the behavior of the pendula and the support becomes irregular (as marked by the curves in the inset). Due to the size of the region, we have recalculated it for higher resolution, as shown in the white enlargement in the figure. The stripes of existence of the irregular attractor indicate that the highest basin stability does not exceed the $p \approx 0.37$ border.

After collecting the basin stability maps of the states generated by model (2), we can apply the procedure discussed in Fig. 1 for any presumed form of the prior parameters distribution. The examples of two possible scenarios are presented in Fig. 3.

First, we consider the classical assumption of the normal Gaussian distribution—the prior PDF is shown in Fig. 3(a). The shape of the two-variate function describes the distribution of random vector $G = (\eta, \Delta)$, where the regions of higher probability are marked with a brighter color (see the density color scale included). In this case, the means for the variables are centered ($\mu_\eta = 1.0$, $\mu_\Delta = 0.5$), with the standard deviations equal to $\sigma_\eta = 0.2$ and $\sigma_\Delta = 0.05$; for simplicity, we consider the uncorrelated configuration, i.e., $\rho_{\eta\Delta} = 0$. The Gaussian assumption for the parameters can be a good starting point if the information on the system characteristics is limited.

By applying the procedure described in Fig. 1, we can update the prior probabilities shown in Fig. 3(a) based on

the basin stability map of any attractor that occurred. The transformation for the in-phase synchronization solution with the beam in the in-phase to the pendula [see the map below the arrow; also Fig. 2(b)] can be found in Fig. 3(b). The shape of the posterior Gaussian probability density function underlines how the prior distribution and the basin stability interplay. As can be seen, the prior PDF has been truncated in the region of the attractor absence ($\eta < 0.8$) and stretched to become similar to the shape of the basin stability map. Moreover, even though the synchronization pattern has the highest stability in the lower domain of Δ values, the most probable parameters should be assumed within higher damping—see the yellow spot in Fig. 3(b)—due to the unimodal character of the prior assumption [the centered peak in Fig. 3(a)].

Understanding the nature of the parameters, one can easily combine various distributions into multivariate cases. In Fig. 3(c), we present the scenario when the prior assumption on the η characteristic is uniform, while the distribution of the Δ one is (independently) considered exponential with the rate of $\lambda = 1.5$; the PDF surface has been scaled to fit the boundaries shown in the figure (the total probability mass equal to one). In this scenario, we assume that the lower damping values are more expected to occur than the higher ones (see the yellow color around $\Delta \approx 0$). The prior uncertainties are updated using the antiphase synchronization pattern [see the basin stability map below the arrow; also Fig. 2(a)], which results in the posterior exponential probability surface presented in Fig. 3(d). As can be seen, the density has become highly squeezed around $\eta = 0.8$, where the probability of the attractor appearance is the highest (see the yellow funnel in the basin stability map). However, the PDF flattens with the increase of the damping (even though the pattern is possible also for high Δ values), due to the prior assumptions on the parameters.

The results discussed in Fig. 3 uncover the possibilities for updating system uncertainties using formula (6) and the basin stability concept. The proper estimation of the latter one is crucial, since the case of zero stability (the absence of the attractor for given parameters) excludes the point from the posterior distribution. To underline this problem, we have studied the system close to the ragged border of the existence of desynchronization solution shown in Fig. 2(d) (see the enlargement in the inset included). The results of our investigations are discussed in Figs. 4 and 5.

Let us focus on parameter point $(\eta^*, \Delta^*) = (0.70875, 0.015)$ for which the desynchronized state is possible. We have split the neighborhood of the considered point (the parameter space) into a 3×3 matrix of cells, schematically shown in the inset included in Fig. 4 (see the right lower corner). In this setup, the (η^*, Δ^*) point (marked in grey) is always centered within the middle cell, while the horizontal (vertical) length of the mesh is equal to $2\tilde{\eta}/2\tilde{\Delta}$. The size of the matrix can be manipulated (shortened) using indicator $j \in \{0, \dots, 127\}$ in the following way: $\tilde{\eta} = 0.008 - j \cdot 6.25 \times 10^{-5}$ and $\tilde{\Delta} = 0.0032 - j \cdot 2.5 \times 10^{-5}$. The smaller the mesh (for bigger j), the closer the cells are accumulated around the (η^*, Δ^*) center; for $j = 128$, the matrix reduces to a singular point. Investigating basin stability for the cells using different j values, we can observe how the probabilities change when

the structure of the (desynchronization) attractor domain is complex.

Using the classical approach, we approximate the basin stability value within the map cell using fixed parameters (typically, the ones from the cell center). The result of such a procedure is marked by the green solid curve in Fig. 4, which corresponds to points $(\eta^* + 2\tilde{\eta}/3, \Delta^*)$ —see the green hyphen in the matrix inset. When the mesh is big, the estimated basin stability (parameter p) remains zero, as can be seen for $j \lesssim 64$. Getting closer to the (grey) center, we observe the spike of probability which converges to the $\hat{p} = 0.272$ limit as $j \rightarrow 128$ [the basin stability of the (η^*, Δ^*) point, marked by the grey horizontal line]. On the other hand, we have approximated the probability within the map cell using different approaches of varied parameters, i.e., uniformly randomizing parameters from the green hatched region for each trial (see the inset in Fig. 4). The basin stability curve corresponding to this method has been presented as the green dashed one, and even for $j = 0$ it starts from a nonzero value. In this scenario, the probability generally increases, indicating that the desynchronized state can occur more often when we reduce the size of the cell.

The comparison between the discussed methods underlines that the one with parameters varied can become superior in the presence of uncertainties. When the exact values of the parameters are unknown, by varying them within the map cell we limit the possibility of omitting the attractor (which can happen when the parameters are fixed outside the solution domain due to its complex structure). This problem has been presented in Fig. 5, where in the left column we present the results obtained for the classical approach (parameters fixed), and in the middle one the results using varied parameters; the absolute difference between the results obtained using both methods is included in the right column for comparison. Each of the matrices included in Fig. 5 corresponds to the 3×3 mesh shown in the inset of Fig. 4, with different values of parameters $\tilde{\eta}$ and $\tilde{\Delta}$. The latter ones are determined using the j index marked around each matrix ($j = 0, 60, 90$) and the formulas $\tilde{\eta} = 0.008 - j \cdot 6.25 \times 10^{-5}$ and $\tilde{\Delta} = 0.0032 - j \cdot 2.5 \times 10^{-5}$; for example, the boxes presented in Fig. 5 (b) for $j = 60$ correspond to the parameter region $(\eta, \Delta) \in [0.70875 - (0.008 - 60 \times 6.25 \times 10^{-5}), 0.70875 + (0.008 - 60 \times 6.25 \times 10^{-5})] \times [0.015 - (0.0032 - 60 \times 2.5 \times 10^{-5}), 0.015 + (0.0032 - 60 \times 2.5 \times 10^{-5})]$, split into evenly partitioned 3×3 mesh. The percentage results included in each cell denote the estimations of the basin stability of the desynchronization solution within chosen parameters regime. For easier comparison, the results are accompanied with colors (shades of blue) where the darker the color, the higher the probability (the scenarios of zero basin stability have been left blank). Moreover, we denote the grid elements using integer numbers (0, 1, 2 in the horizontal and the vertical axis of the matrices) for simpler reference in the text—see further description for details.

Starting from the largest matrix for $j = 0$ —Fig. 5(a)—we can already observe that the estimations for the (0, 1) and the (2, 2) blocks highly differ. The classical method indicates the attractor absence (the cells left blank), while the one using variations, basins stabilities around 8 – 10% (which satisfies typical confidence intervals for potential hypothesis testing).

The attractor ragged domain intersects with the considered cells, and when the parameters are uncertain (or become perturbed), the state can spontaneously occur—we lose this information using the classical approach of fixed parameters. Reducing matrix size twice [Fig. 5(b) for $j = 60$], we can still observe this problem: Here, for the (2, 1) cell (no attractor vs $p = 8.1\%$) but also for the (0, 0) block, where the probabilities highly differ between the methods (0.3% vs 5.5%). Decreasing the mesh further for $j = 90$ in Fig. 5(c), all the basin stabilities become nonzero, but we can still notice some significant discrepancies between the results, e.g., $p = 0.9\%$ (left) and $p = 6.6\%$ (right) for the (2, 0) block.

The proposed method of parameter variation can also become a good approximation for the classical approach when the attractor exists everywhere within the map cell. This scenario is presented in Fig. 4 for the block hatched in orange and corresponds to the dashed curve of the same color. The estimations of basin stability fluctuate around the original $\hat{p} = 0.272$ value, starting below it (underestimation) but successively converging as the j indicator increases. We have also compared the approaches for the general case, i.e., using all the cells from the considered parameter matrix. In this case, the variation method randomly picks the coefficients from the $[\eta^* - \tilde{\eta}, \eta^* + \tilde{\eta}] \times [\Delta^* - \tilde{\Delta}, \Delta^* + \tilde{\Delta}]$ domain, while the classical way determines basin stability as the mean of nine central points of the cells creating the matrix [e.g., for the left upper block, the parameters are considered fixed at $(\eta^* - 2\tilde{\eta}/3, \Delta^* + 2\tilde{\Delta}/3)$]. The results are shown using the black curves (classical method: solid; variation method, dashed) in the inset in Fig. 4. As one can see, even though the estimations for the separate cells differed previously (see Fig. 5 for details), the averaged results are very similar and converge to the limit with a similar slope. Naturally, the described observance should not be generalized, as it highly depends on the structure of the attractor existence region and the basin stability distribution within it.

III. CONCLUSIONS

In conclusion, the procedure discussed in this paper allows us to use the basin stability tool and fundamental probability laws to update prior knowledge on the system parameters. As we have shown, depending on the attractor that occurs, we can obtain various transformations of the presumed distribution, which is influenced by the structure of corresponding basin stability map. The posterior result gives more insights on

the conditions leading to the occurrence of a particular state, as it combines both the information on its stability and the assumed distribution of coefficients. Using the Bayesian inference, we can distinguish the regions in the parameter space where particular types of solutions are more (or less) probable, possibly controlling their occurrence with higher accuracy if desired or required. The proposed procedure can also be used to update our knowledge on the conditions that have led to the appearance of a particular behavior (the domains with the highest probability) and predict it in future.

To account for uncertainties, we also propose an approach for practical evaluation of basin stability maps, involving the variation of parameters. The method is robust on spontaneous (small) inaccuracies in the system working conditions and can be more appropriate (then the classical approach) when some of the states are undesired and their occurrence should be highly controlled in the terms of probability. The procedure presented for the mechanical setup with various coexisting synchronous patterns (also the desynchronized state) can be applied to any multistable system with prior parameters assumptions and basin stability maps of possible attractors. The computational (numerical) effort required by the discussed concept refers to the calculation of the basin stability maps only. The maps should be determined for every possible state of the system and their resolution should be sufficient to take into account possible variations of parameters. When the basin stabilities are already calculated, the procedure described in Fig. 1 can be applied to any chosen prior parameter distribution. The computational cost of obtaining the posterior PDF is limited, since the shape of the density function is always modeled by formula (6). Assuming that the basin stability maps for a chosen system are already given, one can examine various prior parameters assumptions and obtain the posterior probability functions without recalculating the basin stability maps for every simulation.

For crucial models of complex phenomena, updating system uncertainties using Bayesian inference can become an essential key for understanding the occurrence of particular behaviours and their further studies.

ACKNOWLEDGMENTS

This paper has been supported by the National Science Centre, Poland, OPUS Programmes (Projects No. 2018/29/B/ST8/00457 and No. 2021/43/B/ST8/00641).

-
- [1] P. J. Menck, J. Heitzig, N. Marwan, and J. Kurths, How basin stability complements the linear-stability paradigm, *Nat. Phys.* **9**, 89 (2013).
 - [2] N. Wunderling, M. Gelbrecht, R. Winkelmann, J. Kurths, and J. F. Donges, Basin stability and limit cycles in a conceptual model for climate tipping cascades, *New J. Phys.* **22**, 123031 (2020).
 - [3] W. Wei, W. Xu, Y. Song, and J. Liu, Bifurcation and basin stability of an SIR epidemic model with limited medical resources and switching noise, *Chaos Solit. Fractals* **152**, 111423 (2021).
 - [4] D. Pattanayak, A. Mishra, S. K. Dana, and N. Bairagi, Bistability in a tri-trophic food chain model: Basin stability perspective, *Chaos* **31**, 073124 (2021).
 - [5] S. Rakshit, B. K. Bera, S. Majhi, C. Hens, and D. Ghosh, Basin stability measure of different steady states in coupled oscillators, *Sci. Rep.* **7**, 45909 (2017).
 - [6] P. Brzeski, M. Lazarek, T. Kapitaniak, J. Kurths, and P. Perlikowski, Basin stability approach for quantifying responses of multistable systems with parameters mismatch, *Meccanica* **51**, 2713 (2016).

- [7] O. V. Maslennikov, V. I. Nekorkin, and J. Kurths, Basin stability for burst synchronization in small-world networks of chaotic slow-fast oscillators, *Phys. Rev. E* **92**, 042803 (2015).
- [8] S. Leng, W. Lin, and J. Kurths, Basin stability in delayed dynamics, *Sci. Rep.* **6**, 21449 (2016).
- [9] H. Zhang, W. Xu, Y. Lei, and Y. Qiao, Early warning and basin stability in a stochastic vegetation-water dynamical system, *Commun. Nonlinear Sci. Numer. Simul.* **77**, 258 (2019).
- [10] A. van Kan, J. Jegminat, J. F. Donges, and J. Kurths, Constrained basin stability for studying transient phenomena in dynamical systems, *Phys. Rev. E* **93**, 042205 (2016).
- [11] S. Rakshit, B. K. Bera, M. Perc, and D. Ghosh, Basin stability for chimera states, *Sci. Rep.* **7**, 2412 (2017).
- [12] P. Schultz, J. Heitzig, and J. Kurths, Detours around basin stability in power networks, *New J. Phys.* **16**, 125001 (2014).
- [13] P. J. Menck, J. Heitzig, J. Kurths, and H. Joachim Schellnhuber, How dead ends undermine power grid stability, *Nat. Commun.* **5**, 3969 (2014).
- [14] Z. Liu, X. He, Z. Ding, and Z. Zhang, A basin stability based metric for ranking the transient stability of generators, *IEEE Trans. Ind. Inform.* **15**, 1450 (2019).
- [15] Z. Liu and Z. Zhang, Quantifying transient stability of generators by basin stability and Kuramoto-like models, in *2017 North American Power Symposium (NAPS)* (IEEE, Piscataway, NJ, 2017), pp. 1–6.
- [16] A. N. Montanari, E. I. Moreira, and L. A. Aguirre, Effects of network heterogeneity and tripping time on the basin stability of power systems, *Commun. Nonlinear Sci. Numer. Simul.* **89**, 105296 (2020).
- [17] P. Ji and J. Kurths, Basin stability of the Kuramoto-like model in small networks, *Eur. Phys. J. Spec. Top.* **223**, 2483 (2014).
- [18] H. Kim, S. H. Lee, and P. Holme, Building blocks of the basin stability of power grids, *Phys. Rev. E* **93**, 062318 (2016).
- [19] Y. Feld and A. K. Hartmann, Large-deviations of the basin stability of power grids, *Chaos* **29**, 113103 (2019).
- [20] P. Schultz, F. Hellmann, K. N. Webster, and J. Kurths, Bounding the first exit from the basin: Independence times and finite-time basin stability, *Chaos* **28**, 043102 (2018).
- [21] C. Mitra, A. Choudhary, S. Sinha, J. Kurths, and R. V. Donner, Multiple-node basin stability in complex dynamical networks, *Phys. Rev. E* **95**, 032317 (2017).
- [22] P. Ji, W. Lu, and J. Kurths, Stochastic basin stability in complex networks, *Europhys. Lett.* **122**, 40003 (2018).
- [23] P. Brzeski, J. Wojewoda, T. Kapitaniak, J. Kurths, and P. Perlikowski, Sample-based approach can outperform the classical dynamical analysis—experimental confirmation of the basin stability method, *Sci. Rep.* **7**, 6121 (2017).
- [24] Y. Wu, Z. Song, W. Liu, J. Jia, and J. Xiao, Experimental and numerical study on the basin stability of the coupled metronomes, *Eur. Phys. J. Spec. Top.* **223**, 697 (2014).
- [25] Y. Che and C. Cheng, Active learning and relevance vector machine in efficient estimate of basin stability for large-scale dynamic networks, *Chaos* **31**, 053129 (2021).
- [26] Y. Che, C. Cheng, Z. Liu, and Z. Zhang, Fast basin stability estimation for dynamic systems under large perturbations with sequential support vector machine, *Physica D* **405**, 132381 (2020).
- [27] C. Nauck, M. Lindner, K. Schürholt, H. Zhang, P. Schultz, J. Kurths, I. Isenhardt, and F. Hellmann, Predicting basin stability of power grids using graph neural networks, *New J. Phys.* **24**, 043041 (2022).
- [28] P. Schultz, P. J. Menck, J. Heitzig, and J. Kurths, Potentials and limits to basin stability estimation, *New J. Phys.* **19**, 023005 (2017).
- [29] K. Czołczyński, P. Perlikowski, A. Stefański, and T. Kapitaniak, Why two clocks synchronize: Energy balance of the synchronized clocks, *Chaos* **21**, 023129 (2011).
- [30] M. Kapitaniak, K. Czołczyński, P. Perlikowski, A. Stefański, and T. Kapitaniak, Synchronization of clocks, *Phys. Rep.* **517**, 1 (2012).
- [31] D. Dudkowski, K. Czołczyński, and T. Kapitaniak, Multistability and basin stability in coupled pendulum clocks, *Chaos* **29**, 103140 (2019).
- [32] S. N. Chowdhury, A. Ray, S. K. Dana, and D. Ghosh, Extreme events in dynamical systems and random walkers: A review, *Phys. Rep.* **966**, 1 (2022).